

LETTER • OPEN ACCESS

Satellite-based solar-induced fluorescence tracks seasonal and elevational patterns of photosynthesis in California's Sierra Nevada mountains

To cite this article: Lewis Kunik *et al* 2024 *Environ. Res. Lett.* **19** 014008

View the [article online](#) for updates and enhancements.

You may also like

- [Photosynthetic productivity and its efficiencies in ISIMIP2a biome models: benchmarking for impact assessment studies](#)

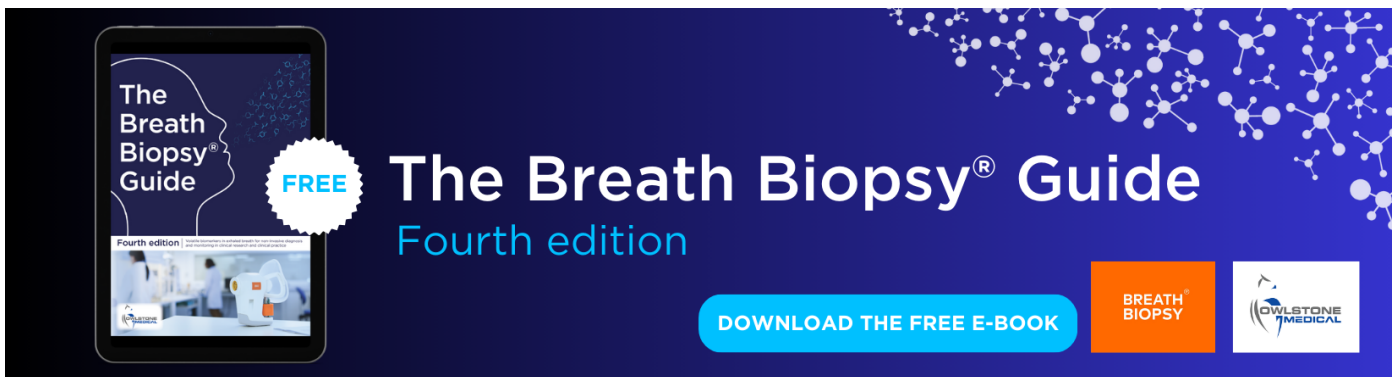
Akihiko Ito, Kazuya Nishina, Christopher P O Reyer *et al.*

- [Below-surface water mediates the response of African forests to reduced rainfall](#)

Nima Madani, John S Kimball, Nicholas C Parazoo *et al.*

- [Exposure to cold temperature affects the spring phenology of Alaskan deciduous vegetation types](#)

Mingjie Shi, Nicholas C Parazoo, Su-Jong Jeong *et al.*



The Breath Biopsy® Guide
Fourth edition

FREE

BREATH BIOPSY

OWLSTONE MEDICAL

ENVIRONMENTAL RESEARCH LETTERS



OPEN ACCESS

RECEIVED
11 August 2023

REVISED
19 October 2023

ACCEPTED FOR PUBLICATION
26 October 2023

PUBLISHED
30 November 2023

Original content from
this work may be used
under the terms of the
[Creative Commons
Attribution 4.0 licence](#).

Any further distribution
of this work must
maintain attribution to
the author(s) and the title
of the work, journal
citation and DOI.



LETTER

Satellite-based solar-induced fluorescence tracks seasonal and elevational patterns of photosynthesis in California's Sierra Nevada mountains

Lewis Kunik¹ , David R Bowling^{1,2} , Brett Raczka³ , Christian Frankenberg^{4,5} , Philipp Köhler⁶ , Rui Cheng⁷ , Kenneth R Smith² , Michael Goulden⁸ , Martin Jung⁹ and John C Lin^{1,*}

¹ Department of Atmospheric Sciences, University of Utah, Salt Lake City, UT, United States of America

² School of Biological Sciences, University of Utah, Salt Lake City, UT, United States of America

³ Computational and Information Systems Laboratory, National Center for Atmospheric Research, Boulder, CO, United States of America

⁴ Division of Geological and Planetary Sciences, California Institute of Technology, Pasadena, CA, United States of America

⁵ Jet Propulsion Laboratory, California Institute of Technology, Pasadena, CA, United States of America

⁶ Remote Sensing and Products Division, EUMETSAT, Darmstadt, Germany

⁷ Department of Civil and Environmental Engineering, Massachusetts Institute of Technology, Cambridge, MA, United States of America

⁸ Department of Earth System Science, University of California-Irvine, Irvine, CA, United States of America

⁹ Department of Biogeochemical Integration, Max Planck Institute for Biogeochemistry, Jena, Germany

* Author to whom any correspondence should be addressed.

E-mail: john.lin@utah.edu

Keywords: solar-induced fluorescence (SIF), gross primary productivity (GPP), elevation gradient, topography, community land model (CLM), FLUXCOM, carbon monitoring systems

Supplementary material for this article is available [online](#)

Abstract

Robust carbon monitoring systems are needed for land managers to assess and mitigate the changing effects of ecosystem stress on western United States forests, where most aboveground carbon is stored in mountainous areas. Atmospheric carbon uptake via gross primary productivity (GPP) is an important indicator of ecosystem function and is particularly relevant to carbon monitoring systems. However, limited ground-based observations in remote areas with complex topography represent a significant challenge for tracking regional-scale GPP. Satellite observations can help bridge these monitoring gaps, but the accuracy of remote sensing methods for inferring GPP is still limited in montane evergreen needleleaf biomes, where (a) photosynthetic activity is largely decoupled from canopy structure and chlorophyll content, and (b) strong heterogeneity in phenology and atmospheric conditions is difficult to resolve in space and time. Using monthly solar-induced chlorophyll fluorescence (SIF) sampled at \sim 4 km from the TROPOspheric Monitoring Instrument (TROPOMI), we show that high-resolution satellite-observed SIF followed ecological expectations of seasonal and elevational patterns of GPP across a 3000 m elevation gradient in the Sierra Nevada mountains of California. After accounting for the effects of high reflected radiance in TROPOMI SIF due to snow cover, the seasonal and elevational patterns of SIF were well correlated with GPP estimates from a machine-learning model (FLUXCOM) and a land surface model (CLM5.0-SP), outperforming other spectral vegetation indices. Differences in the seasonality of TROPOMI SIF and GPP estimates were likely attributed to misrepresentation of moisture limitation and winter photosynthetic activity in FLUXCOM and CLM5.0 respectively, as indicated by discrepancies with GPP derived from eddy covariance observations in the southern Sierra Nevada. These results suggest that satellite-observed SIF can serve as a useful diagnostic and constraint to improve upon estimates of GPP toward multiscale carbon monitoring systems in montane, evergreen conifer biomes at regional scales.

1. Introduction

Temperate forests play a critical role in the terrestrial carbon cycle, accounting for 25% of the world's forested area and 37% of the global carbon uptake (Adams *et al* 2019). In the coming decades, warming and drying trends are expected to continue in temperate regions, including the western United States (US) (IPCC 2023), suggesting dramatic changes to vegetation water and nutrient cycling over relatively short ecological timescales. Yet, the implications for forest carbon reserves are still unclear, particularly within heterogeneous montane environments (Rotach *et al* 2014), which hold the majority of aboveground biomass in the western US (Schimel *et al* 2002, Schimel and Braswell 2005). Higher mean temperatures and atmospheric CO₂ concentrations generally enhance gross carbon uptake. However, increased water limitations may negate these effects (e.g. Angert *et al* 2005) while increasing the susceptibility of forests to drought-induced disturbance. This is particularly relevant in the western US mountains, where a 25% decline in total snowpack is expected by 2050, presaging a possible 'low-to-no-snow' future, which would involve critical changes to vegetation water use and physiological demands along topographic gradients (Siirila-Woodburn *et al* 2021). The impact on carbon cycle modeling, forest management and development along the wildland urban interface would be highly consequential, given the increasing interactions between drought, insect outbreaks and wildfires in the western US (Clark *et al* 2016, Fettig *et al* 2021).

Monitoring the forest carbon cycle is essential to understand the functional changes that accompany increasing water stress and shifting disturbance regimes. Gross primary productivity (GPP; gross photosynthetic carbon uptake by plants) represents a key monitoring indicator of ecosystem health and function. Eddy covariance (EC) towers, which measure land–atmosphere carbon exchange, are currently the most effective method for estimating GPP at the canopy scale (Baldocchi 2008), representing an average fetch of several hundred meters (Chu *et al* 2021). However, resource limitations have led to the spatial underrepresentation of flux measurement sites in the remote, temporally variable and heterogeneous terrain of many western US forests. Considering this and other challenges of the EC technique in complex topography, ground-based measurements alone do not constitute a sufficient regional monitoring strategy in the western US.

Satellite observations can provide more complete information at the landscape scale, particularly when used in concert with ground-based tower measurements. In remote sensing, GPP is often quantified

using the light use efficiency (LUE) model (Monteith 1972):

$$GPP = APAR * LUE \quad (1)$$

where the photosynthetically active radiation absorbed by the plant leaf (APAR) may be estimated using ratios of surface reflectance, and the LUE of carbon assimilation is inferred empirically based on plant functional type. Traditional reflectance-based methods, such as the Normalized Difference Vegetation Index (NDVI) and the Enhanced Vegetation Index (EVI), rely on the linkage of APAR to chlorophyll content and forest canopy structure (seasonality of green leaf area) to infer GPP. However, over 90% of the forests in the western US are predominantly evergreen needleleaf forest (ENF) (Oswalt *et al* 2019), for which the chlorophyll content and canopy structure are seasonally invariant, rendering these models ineffective for observing temporal changes in GPP over these regions (Magney *et al* 2019, Pierrat *et al* *in review*).

An alternative observation method exploits a mechanistic linkage between photochemical yield and the emission of chlorophyll fluorescence, as detected by spaceborne spectrometers ('solar-induced fluorescence' (SIF)):

$$GPP = SIF * \frac{LUE}{\Phi_F \times f_{esc}} \quad (2)$$

where Φ_F is the effective fluorescence yield, and f_{esc} is the escape ratio of SIF from the canopy (Guanter *et al* 2014, Zeng *et al* 2019). A strong empirical relationship between SIF and GPP in ENF ecosystems has been documented from tower (Magney *et al* 2019) to regional scales (Frankenberg *et al* 2011, Walther *et al* 2016, Sun *et al* 2017, Zuromski *et al* 2018), where recent advances in satellite remote sensing have given way to high-resolution SIF datasets (Köhler *et al* 2018, Sun *et al* 2018). At scales of a few kilometers, satellite SIF has been shown to be insensitive to spatial variations in surface reflectance over complex surface geometries (Cheng *et al* 2022a), indicating a promising utility of SIF to explore spatial, seasonal and interannual patterns of photosynthesis in heterogeneous mountain terrain.

Despite strong evidence for SIF as an effective proxy for GPP, questions remain about the nature of the SIF–GPP relationship within complex terrain. Recent studies of ENF biomes have highlighted the nonuniformity of SIF–GPP scaling across seasons (Pierrat *et al* 2022, Yang *et al* 2022) and elevation-dependent land cover (Cheng *et al* 2022b). There is considerable debate surrounding the utility of SIF observations to detect changes in GPP due to seasonal or interannual drought (Sun *et al* 2015, Helm *et al* 2020, Marrs *et al* 2020, Butterfield *et al* 2023).

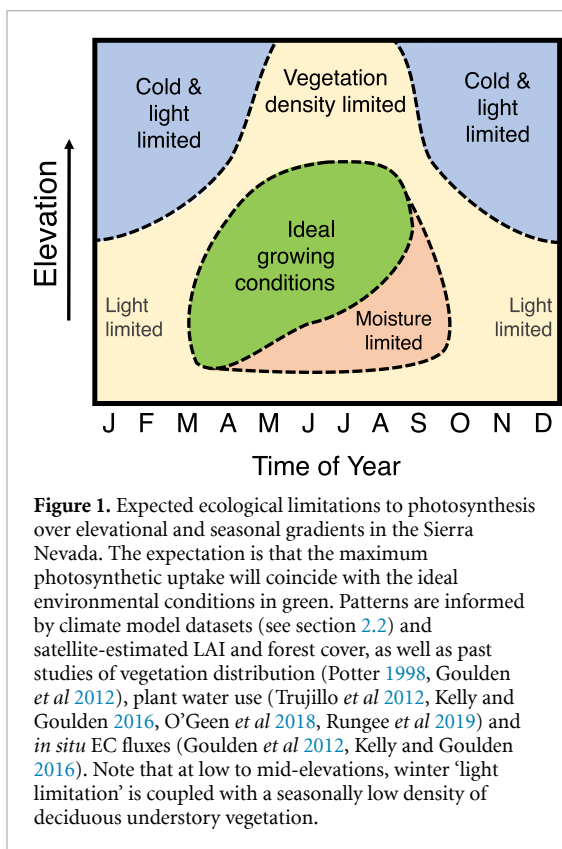


Figure 1. Expected ecological limitations to photosynthesis over elevational and seasonal gradients in the Sierra Nevada. The expectation is that the maximum photosynthetic uptake will coincide with the ideal environmental conditions in green. Patterns are informed by climate model datasets (see section 2.2) and satellite-estimated LAI and forest cover, as well as past studies of vegetation distribution (Potter 1998, Goulden *et al* 2012), plant water use (Trujillo *et al* 2012, Kelly and Goulden 2016, O'Geen *et al* 2018, Rungee *et al* 2019) and *in situ* EC fluxes (Goulden *et al* 2012, Kelly and Goulden 2016). Note that at low to mid-elevations, winter 'light limitation' is coupled with a seasonally low density of deciduous understory vegetation.

For large mountain regions that span multiple climate zones and biome types, these uncertainties have yet to be investigated for their impact on regional estimates. However, understanding the limitations imposed by mountain topography on SIF–GPP relationships could better inform the scale at which biogeochemical stress indicators and disturbance precursors can be detected by satellites.

California's Sierra Nevada mountain range ('the Sierra Nevada') is an ideal domain to explore these questions, where conifer forests spanning over 3000 m in elevation have long been the focus of hydrological, biogeochemical and disturbance studies. Here, a mosaic of grass, shrub and low-density woodlands at low elevations gives way to dense, closed-canopy mixed conifer stands at mid-elevations (high leaf area index (LAI)), with reduced density near the high-elevation timberline (lower LAI) (Potter 1998, Goulden *et al* 2012). Sierra Nevada ecosystems exhibit summer water limitation below approximately 2000 m elevation and winter energy limitation above this elevation threshold (Trujillo *et al* 2012), with year-round photosynthesis occurring around the 2000 m elevation threshold, supported by deep-rooting regolith access (Kelly and Goulden 2016, O'Geen *et al* 2018, Rungee *et al* 2019). The timing of peak GPP in the Sierra Nevada has been shown to follow these patterns, ranging from spring at low elevations to mid-summer at high elevations (Goulden *et al* 2012, Kelly and Goulden 2016). Figure 1 synthesizes findings from past studies,

summarizing the ecological expectations of GPP across seasonal and elevational gradients in the Sierra Nevada, as shaped by climatological and structural controls.

In this study, we evaluate the utility of high-resolution satellite-observed SIF in detecting GPP across the seasonal and elevational gradients of the Sierra Nevada. We seek to assess SIF against the ecological expectations of photosynthesis by comparing SIF with GPP from EC flux towers, a gridded model-data product (FLUXCOM) and a land surface model (CLM5.0). We discuss the limitations of SIF and GPP estimates while highlighting the advantages of SIF over other vegetation indices, presenting opportunities for the use of SIF in the carbon monitoring of montane ENFs.

2. Data and methods

A summary of the datasets and processing methods used in this study is presented in table 1. Additional information concerning the datasets and their analysis is presented as follows.

2.1. Sierra Nevada study domain and land cover

Our study domain encompassed 28 700 km² of ENF within California's Central and Southern Sierra Nevada, covering an altitudinal gradient ranging from 300 to 3400 m above sea level (NOAA ETOPO1 elevation model shown in figure 2(a)). The climate is montane Mediterranean; most annual precipitation falls during winter when rain–snow transitions are around 2000–2500 m in elevation (Shulgina *et al* 2023). The European Space Agency's (ESA) Climate Change Initiative land cover dataset (Hollman *et al* 2013) was used to define the ENF domain boundaries; areas of other prevailing land cover types were omitted from this analysis (see table 1).

2.2. Gridded SIF, GPP, modeled climate and vegetation indices

Individual SIF retrievals from TROPOMI (the single payload of the ESA Sentinel-5 Precursor satellite) soundings were gridded to a monthly time resolution and 0.04° spatial resolution, which oversampled the native 7 × 5 km resolution. Instantaneous SIF values at 740 nm were scaled to daily mean values (often denoted as SIF_{dc} but herein denoted as SIF for simplicity), as described by Köhler *et al* (2018). The SIF data were further corrected to account for the effects of surface geometry on solar incidence angle (Cheng *et al* 2022a), which are minimal on average (3% mean difference over domain) but can reach up to 92% for some grid cells in the winter months. To minimize noise from high reflected radiance over snowy surfaces, we used MODIS monthly snow cover (MOD10CM) to filter out pixels with high snow cover. The spatial pattern of the mean annual

Table 1. Overview of datasets and methods used in this study.

Data variable	Data source	Original resolution		Time range	Description	References
		Spatial ^a	Temporal			
Gridded datasets						
SIF	TROPOMI (Sentinel 5 Precursor)	7 km × 5 km	Monthly	2018 (February)–2021 (July)	See section 2.2. Data were oversampled from original spatial resolution to 0.04° for this study.	Köhler <i>et al</i> 2018, Cheng <i>et al</i> 2022a
GPP	FLUXCOM	0.0833°	8-daily, monthly	2009–2020	—	Jung <i>et al</i> 2020
Elevation	NOAA/NESDIS ETOPO1 Global Relief	1 arc second	n/a	n/a	—	Amante and Eakins 2009
Land cover	European Space Agency Climate Change Initiative	300 m	Annual	2019	300 m land use categorization data from the most recent available year (2019) were quantified as 1 (ENF) or 0 (not ENF) and interpolated to 0.04° to estimate the percentage ENF coverage. The ENF domain mask was defined as grid cells with >50% ENF coverage.	Hollman <i>et al</i> 2013
Snow cover fraction	Terra MODIS MOD10CM.061	0.05°	Monthly	Same as TROPOMI SIF	Snow cover was expressed as the percentage of the land surface covered by snow per grid cell. TROPOMI SIF data were omitted if the corresponding snow cover fraction was >50% due to interference from high reflected radiance.	Hall <i>et al</i> 2021
Air temperature (daily mean)	GRIDMET	1/24°	3-hourly	1980–2015	GRIDMET temperature is derived from temporally rich meteorological data from the North American Land Data Assimilation System (NLDAS-2) and high spatial resolution from the parameter-elevation regressions on independent-slopes model.	Mitchell <i>et al</i> 2004, Daly <i>et al</i> 2008, Abatzoglou 2013, Buotte <i>et al</i> 2019
Climatic water deficit (CWD)	TerraClimate	1/24°	Monthly	1980–2021	CWD is defined as the annual evaporative demand that exceeds available soil moisture (potential minus actual evapotranspiration), estimated using the Penman–Monteith approach and Thornthwaite–Mather climatic water balance model.	Abatzoglou <i>et al</i> 2018

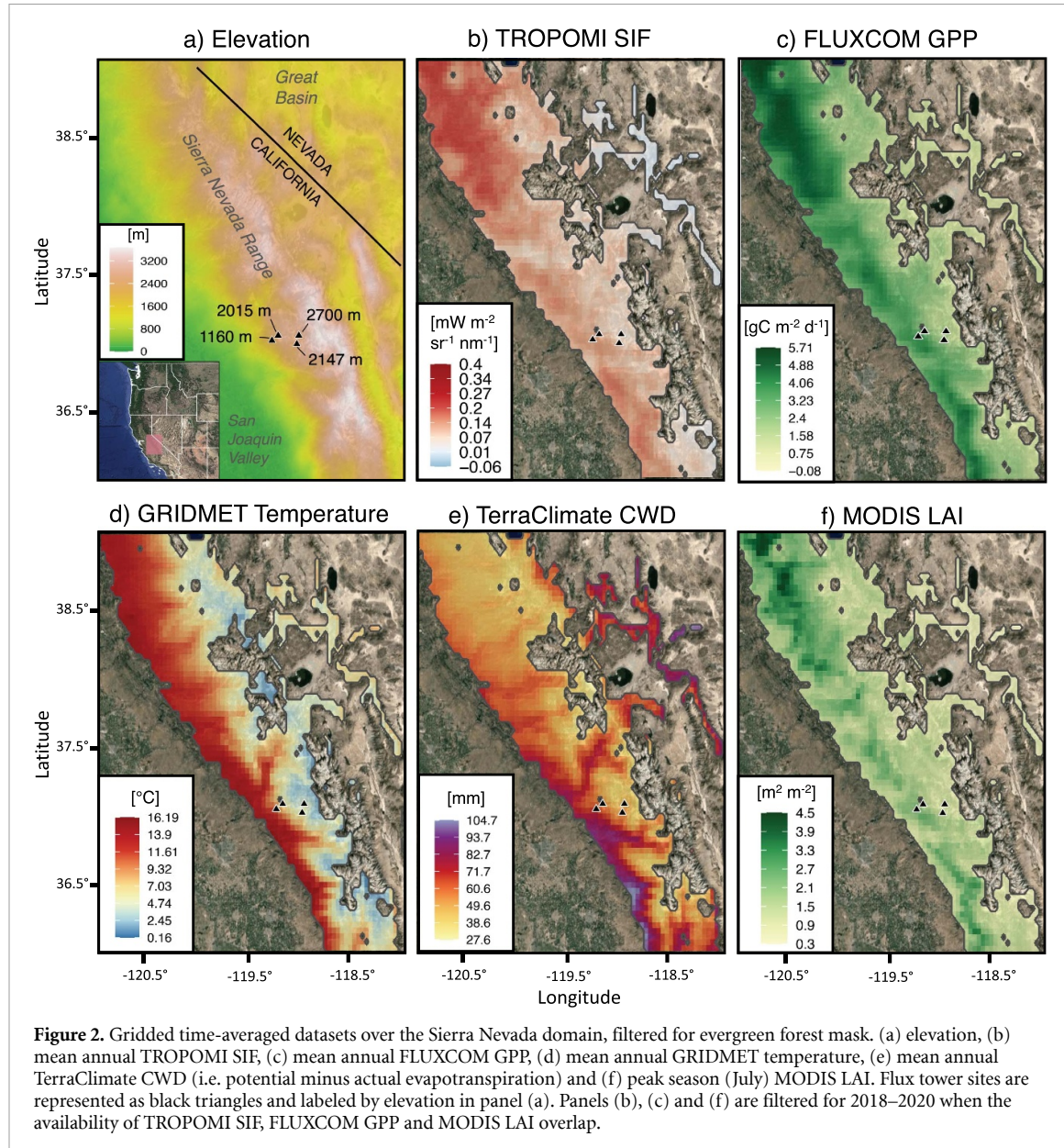
(Continued.)

Table 1. (Continued.)

Data variable	Data source	Original resolution			Description	References
		Spatial ^a	Temporal	Time range		
LAI	Terra + Aqua MODIS MCD15A2H.061	500 m	8-daily	2009–2020	LAI is defined as the one-half total leaf surface area per unit ground area. MODIS LAI was calculated using red and near-infrared surface reflectances as well as empirical relationships of NDVI and LAI.	Myeni <i>et al</i> 2021
Eddy covariance						
US-CZ2 (1160 m)	Sierra Critical Zone Observatory/AmeriFlux	n/a	30 min	2010 (July)–2013 (January) ^b	See section 2.3.	Data collection: Goulden 2018a, 2018b, 2018c; Partitioning: Reichstein <i>et al</i> 2005, Wutzler <i>et al</i> 2018
US-CZ3 (2015 m)				2008 (September)–2016 (October)		
US-CZ4 (2700 m)				2010 (January)–2012 (March)		
NEO-TEAK (2147 m)	National Ecological Observatory Network (NEON)			2018 (July)–2022 (December)		Data collection: Metzger <i>et al</i> 2019; Partitioning: Reichstein <i>et al</i> 2005, Wutzler <i>et al</i> 2018
Land surface model						
GPP (regional)	Community Land Model 5.0	1.96° × 1°	Daily	1980–2015	GPP was simulated under two separate configurations: CLM5.0 with biogeochemistry (CLM5.0-BGC) and CLM5.0 with prescribed leaf and stem area from the MODIS satellite data (CLM5.0-SP). The full model setup is detailed in appendix C.	Lawrence <i>et al</i> 2019, Danabasoglu <i>et al</i> 2020, Racza <i>et al</i> 2021
GPP (site level)		n/a	Daily		Site-specific land cover, forest canopy cover and bedrock depth were defined using the AmeriFlux Biological, Ancillary, Disturbance, and Metadata files	https://ameriflux.lbl.gov/data/badm/

Notes: ^a Gridded datasets were re-rasterized from their original resolution to match the spatial resolution of TROPOMI SIF used in this analysis 0.04°.

^b The time range for US-CZ2 (1160 m) flux data was abbreviated from 2010 to 2013 to account for the effects of disturbance on mean seasonality at the site (see appendix B).



SIF over the region is shown in figure 2(b). To match the grid resolution of TROPOMI SIF, all other gridded data in this study were re-gridded to 0.04° resolution via bilinear interpolation, resulting in a negligible impact on seasonal and elevation patterns across the domain.

We used monthly gridded estimates of GPP from the FLUXCOM-RS ensemble remote-sensing carbon flux product ('FLUXCOM'; Jung *et al* 2020), distributed natively at $1/12^\circ$ ($\sim 0.0833^\circ$) resolution. FLUXCOM is the median of 18 ensemble members, where nine machine-learning methods were used to predict two flux-partitioning variants for GPP. The models were trained using 8-daily MODIS vegetation and moisture reflectance indices along with land surface temperature and radiation as input, as well as data from >200 FLUXNET EC towers (Tramontana *et al* 2016, Pastorello *et al* 2020), excluding the Sierra Nevada sites used in this study.

Daily mean temperature and CWD (defined as reference evapotranspiration minus actual evapotranspiration) were estimated using the GRIDMET and TerraClimate models (Abatzoglou 2013, Abatzoglou *et al* 2018) to serve as additional diagnostics for the temperature and moisture limitations of GPP.

We compared the patterns of SIF and GPP to those of five spectral reflectance-based vegetation indices (NDVI, kNDVI, EVI, EVI2 and near-infrared reflectance of vegetation (NIR_v)) from the MODIS satellite instrument. Details of these comparisons and the datasets used are summarized in appendix A.

2.3. EC flux tower data

EC measurements of net ecosystem exchange (NEE) were taken along with meteorological data from four flux towers along an elevational gradient in the southern Sierra Nevada. These include the AmeriFlux sites

US-CZ2 (1160 m), US-CZ3 (2015 m) and US-CZ4 (2700 m), and the National Ecological Observatory Network's (NEON) TEAK site (2147 m) (table 1 and figure 2(a)).

NEE data were filtered to remove calm periods and then gap-filled using the *REddyProc* package version 1.3.2 in R (Wutzler *et al* 2018). Ecosystem respiration (R_{eco}) was estimated by fitting a temperature sensitivity function from the gap-filled nighttime NEE (Reichstein *et al* 2005) following procedures described by Wutzler *et al* (2018). The half-hourly estimated R_{eco} was subtracted from NEE to obtain GPP and aggregated to monthly timescales to match the timing of TROPOMI. Mismatch between spatial scales of the EC observations (footprint $<1 \text{ km}^2$) and gridded data ($\sim 16 \text{ km}^2$ pixels) is an inherent limitation in heterogeneous terrains (see section 4.3). We specifically accounted for the effects of a localized disturbance event within the 1160 m EC tower footprint by filtering the site's data for time periods when the canopy structure (indicated by MODIS NIR_v) was aligned between the flux tower footprint and TROPOMI grid cell footprint scales. A full description of this methodology is presented in appendix B.

2.4. Land surface model

The Community Land Model 5.0 (CLM5.0; Lawrence *et al* 2019) was used to simulate GPP to serve as both a validation and diagnostic tool for TROPOMI SIF. Simulations were run using two different modules of CLM5.0, one with a prognostic vegetation state and active biogeochemistry (CLM5.0-BGC), and the other with satellite-prescribed phenology from MODIS LAI data (CLM5.0-SP). In this study, regional simulations were forced by GRIDMET meteorology following Racza *et al* (2021) and centered on the Sierra Nevada domain along with site-level simulations at the four flux tower locations described in section 2.3. The model setup is summarized in table 1; configuration and diagnostic analyses are detailed in appendix C.

2.5. Statistical methods

To compare seasonal trends between datasets, we computed the mean seasonal cycle of monthly SIF and GPP as the average across all years specific to each dataset (see table 1). Flux tower GPP was compared against CLM5.0 point simulations as well as gridded TROPOMI SIF and FLUXCOM GPP extracted over the flux tower locations. GPP estimates were averaged monthly to match the monthly SIF observations. We computed the difference in the timing of the peak EC GPP with that of the peak TROPOMI SIF ($t_{\text{EC_peak}} - t_{\text{SIF_peak}}$) and FLUXCOM and CLM5.0 GPP ($t_{\text{EC_peak}} - t_{\text{GPP_peak}}$), including both CLM-BGC and -SP model configurations. A positive (negative) difference indicates that the EC peak occurred later (earlier) than the comparison dataset.

To assess the synchronicity of the seasonal patterns in SIF and GPP, we performed cross-correlation analyses to obtain the time-lag shift (in months) of the maximum correlation between cycles at each flux tower site (denoted as $t_{\text{EC_cycle}} - t_{\text{SIF_cycle}}$ for TROPOMI and $t_{\text{EC_cycle}} - t_{\text{GPP_cycle}}$ for FLUXCOM and CLM5.0). SIF was compared with EC GPP by expressing both quantities as fractions relative to their respective maxima across sites. The coefficient of determination (R^2) was computed for each cycle comparison after applying the time lag.

Seasonal and elevational trends were determined by aggregating monthly average gridded SIF, GPP and climatology datasets into 100 m elevation bins from the elevation model to represent the average gridded value for that elevation band. We also computed the domain-aggregated relative distribution across elevation or season by averaging all gridded SIF and GPPs in elevation (or time), calculating the rolling average using a 100 m (or 2 week) window and dividing by the maximum window-mean value.

3. Results

3.1. Seasonal and elevational patterns of gridded SIF and GPP

The annual mean distributions of TROPOMI SIF and FLUXCOM GPP (figures 2(b) and (c)) followed similar spatial patterns throughout the Sierra Nevada, both resembling the spatial pattern of MODIS LAI (figure 2(f)). The majority of SIF and GPP activity was located in the northern third of the domain (38° – 39° N, figures 2(b) and (c)), where elevations are mostly below 2000 m and LAI is high.

Seasonal and elevational trends of SIF and GPP are shown in figures 3(a)–(d), and trends of temperature and CWD are shown in figures 3(e) and (f). The peak TROPOMI SIF occurred in June at mid-elevations (1000–1500 m), with a smaller April peak at low elevations influenced by the spring growth of herbs, grasses and deciduous shrubs. SIF consistently decreased with elevation above these peak zones and decreased from early summer to fall and winter across all elevations. Tracing the elevation and timing of the 90th percentile range of SIF to the GRIDMET temperature (figure 3(e)) gave a corresponding daily mean range of 18°C – 19°C for the June peak.

Elevational trends of FLUXCOM GPP resembled those of TROPOMI SIF, with a maximum around 1300–1500 m; however, FLUXCOM GPP peaked slightly later than SIF (June–July) and remained high throughout the summer (figure 3(b)). The GRIDMET temperature corresponding to the 90th percentile of FLUXCOM GPP ranged from 17°C to 24°C , which is considerably warmer than the corresponding temperature range for TROPOMI SIF's 90th percentile. Below 750 m, seasonal GPP was reduced after May (similar to TROPOMI); however, FLUXCOM GPP showed more sustained patterns

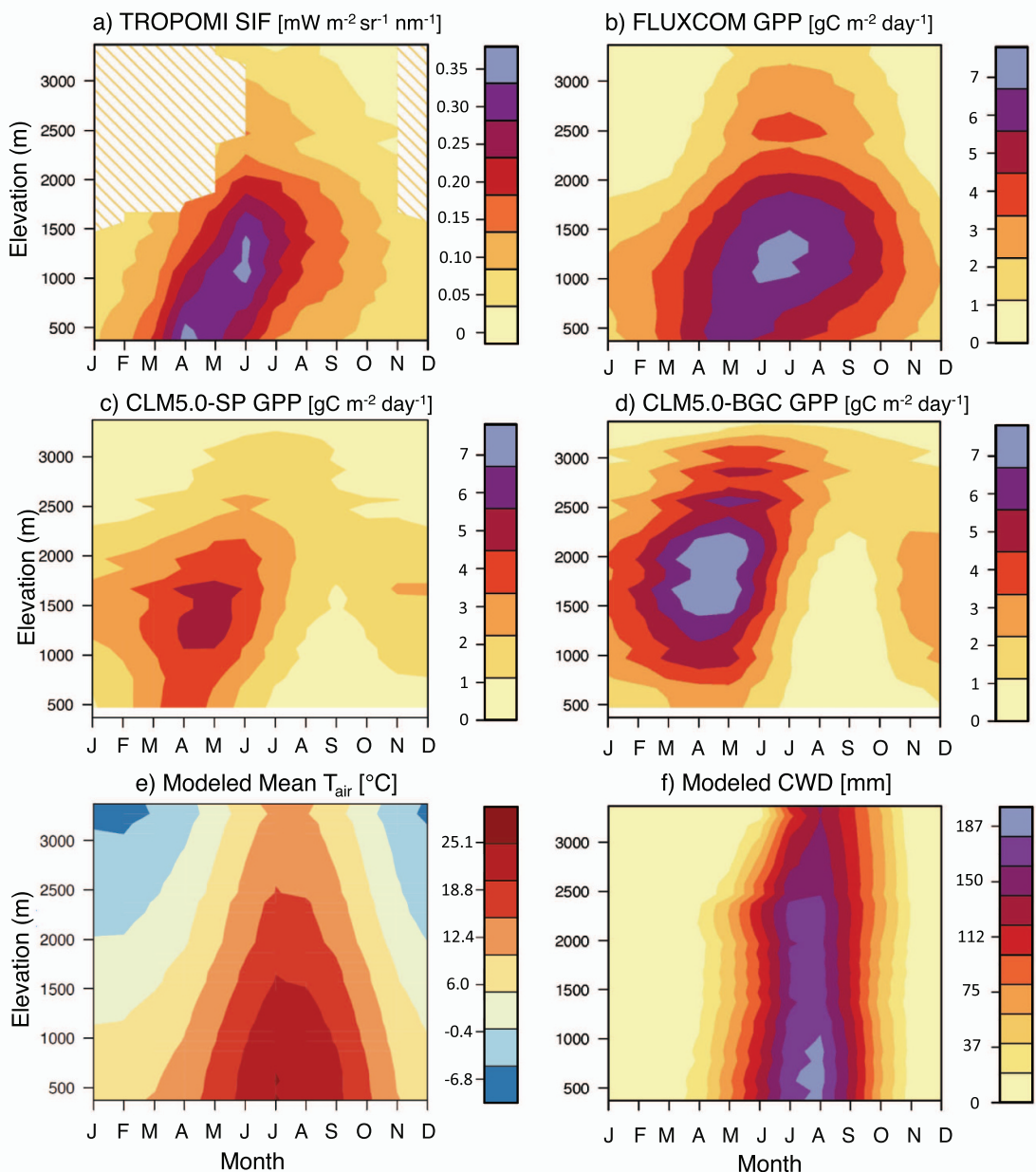


Figure 3. Patterns of gridded datasets and model output over elevation and mean seasonality for (a) TROPOMI SIF, (b) FLUXCOM GPP, (c) simulated CLM5.0-SP GPP, (d) simulated CLM5.0-BGC GPP, (e) GRIDMET model mean temperature and (f) TerraClimate modeled CWD (reference ET—actual ET).

throughout the summer than SIF, extending significant GPP through September at mid-elevations.

CLM5.0-SP simulations also exhibited seasonal and elevational GPP patterns similar to those of FLUXCOM and TROPOMI SIF (figure 3(c)), whereas CLM5.0-BGC simulations differed significantly in magnitude and elevational patterns (figure 3(d)). The CLM5.0-SP peak GPP was lower in magnitude than FLUXCOM GPP, occurring earlier (April–May) but at a similar elevation range (1200–1700 m). CLM5.0-BGC showed a strong, early seasonal GPP peak around March–May at a high elevation band around 1500–2000 m, concomitant with strong, high-elevation patterns in the model LAI (see appendix C). The corresponding mean GRIDMET temperature at

the 90th percentile model GPP ranged from 7 °C to 14 °C for CLM5.0-SP and from 4 °C to 12 °C for CLM5.0-BGC. For both BGC and SP simulations, the peak GPP was slightly delayed with increasing elevation. This was followed by an extensive dormant period from July through November, concurrent with seasonally low soil moisture (appendix C).

3.2. SIF and GPP averaged across time and elevation

Averaging gridded datasets across time allowed us to explore the general relationship between SIF and GPP products and elevation within the Sierra Nevada. TROPOMI SIF and FLUXCOM GPP exhibited similar elevational distributions, with most SIF and GPP

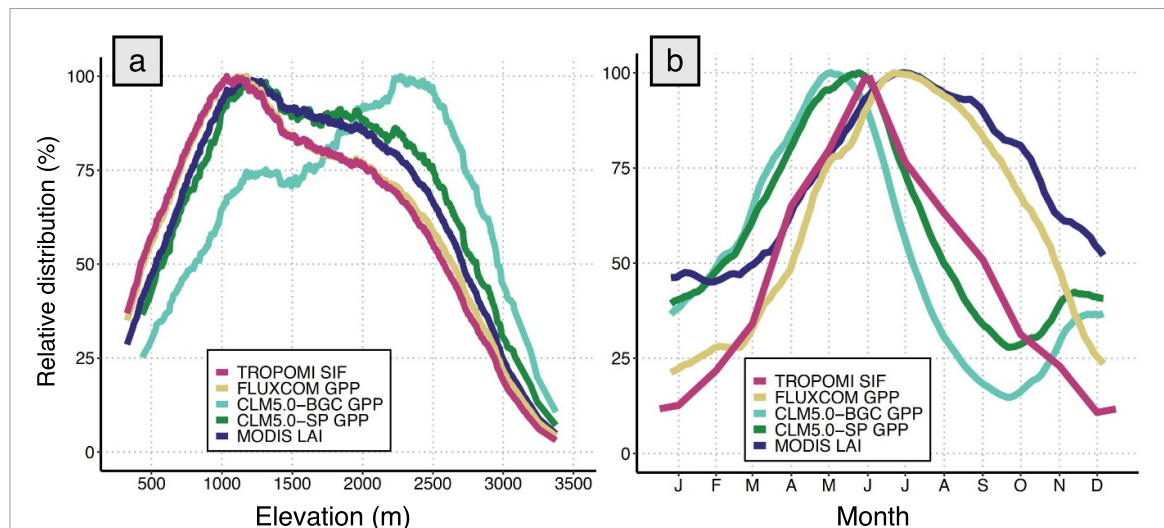


Figure 4. (a) Elevational patterns of annual mean TROPOMI SIF (red), FLUXCOM GPP (yellow), simulated GPP from CLM5.0-BGC (light green), CLM5.0-SP (dark green) and MODIS LAI (navy), separated by elevation bin and expressed as a percentage of the maximum signal over a 100 m moving elevation window. (b) Mean seasonal cycle of spatially aggregated TROPOMI SIF, FLUXCOM GPP, simulated GPP from CLM5.0-BGC, CLM5.0-SP and MODIS LAI (same color scheme as panel (a)), over the full Sierra Nevada domain extent, expressed as a percentage of the maximum signal over a 2 week moving time window.

(above a relative distribution threshold of 80%) distributed between 700 and 1700 m (figure 4(a)). This 80% relative distribution threshold occurred slightly higher for MODIS LAI and CLM5.0-SP GPP, between 800 and 2200 m and 900 and 2400 m elevations, respectively. CLM5.0-BGC GPP was allocated substantially higher in elevation (>80% relative distribution between 1700 and 2700 m), reflecting the impact of prognostic LAI (CLM5.0-BGC) vs. satellite-prescribed LAI (CLM5.0-SP) upon simulated GPP (see appendix C).

Averaged across space, we observed key differences in the seasonality of the datasets (figure 4(b)). Both CLM simulations exhibited a spring increase from January to mid-April, approximately 1.5 months earlier than TROPOMI SIF and FLUXCOM GPP, which increased in near synchrony from mid-February to June. CLM5.0-SP and CLM5.0-BGC GPP declined in response to moisture limitation from May and June, respectively, until both reached seasonal minimums in September and increased again in fall to winter. The domain-averaged TROPOMI SIF peaked sharply in June and then decreased steadily to a seasonal minimum in December. FLUXCOM timing was closely tied to MODIS vegetation indices (figure A2) and diverged from the patterns of SIF and CLM GPP. Both FLUXCOM GPP and LAI were sustained above 75% of the maximum through October and declined toward seasonal minimums in winter, depicting a nearly 2.5 months longer growing season in FLUXCOM GPP than in TROPOMI SIF. Additional MODIS vegetation indices showed little seasonal variation relative to SIF and GPP estimates (figure A2).

3.3. Site-level observations vs. SIF and GPP products

Figure 5 shows the mean seasonal cycle of GPP from the four EC sites compared with gridded SIF, FLUXCOM GPP and CLM5.0 point simulations. Among the models, CLM5.0-SP provided the best match to the seasonal timing and magnitude of EC GPP, whereas CLM5.0-BGC consistently overestimated EC GPP. Both CLM model configurations inadequately captured winter dormancy at the higher elevation sites (2147 and 2700 m) between November and March. Both CLM configurations also showed more dramatic reductions in summer GPP at lower elevations, resulting from seasonal water limitation. FLUXCOM better captured winter dormancy at high elevation sites compared to CLM simulations; however, it showed a positive bias compared to flux towers during summer and fall, particularly at lower elevations. SIF mainly followed the relative patterns of EC GPP; it did not capture winter dormancy at 2147 and 2700 m, but we assumed this to be caused by reflected radiance and thus omitted SIF during periods of snow cover (dashed line). SIF was also low relative to EC GPP at 2700 m because of ‘dilution’ from the non-vegetated terrain within this pixel.

Time series analyses are summarized in table 2, showing lags in the timing of peak signals, as well as the seasonally integrated cross-correlation lags between full seasonal cycles. TROPOMI SIF was consistently within 1 month of EC GPP, considering both peak timing and full seasonal cross correlation. (Lag R^2 values were low at high elevation sites due to lower SIF sample size from snow cover filtering in winter and spring.) The modeled GPP from CLM5.0-SP was also consistently within 1 month of EC GPP.

Table 2. Results of timing analyses of multi-year mean seasonal cycles. $t_{\text{EC,peak}} - t_{\text{SIF,peak}}$ and $t_{\text{EC,peak}} - t_{\text{GPP,peak}}$ are the differences (in months) between peak EC GPP and peak TROPOMI SIF, FLUXCOM GPP or CLM5.0 GPP, $t_{\text{EC,cycle}} - t_{\text{SIF,cycle}}$ and $t_{\text{EC,cycle}} - t_{\text{GPP,cycle}}$ are the lag differences (in months) from cross-correlation analyses, where the lag shown is the timing shift at which EC and SIF, FLUXCOM or CLM5.0 achieve maximum correlation. Lag R^2 values are the coefficients of determination from the cross-correlation function. For all timing differences, negative values indicate that the signal (SIF, FLUXCOM or CLM5) is delayed from the EC GPP cycle; positive values indicate that the signal is ahead of the EC GPP cycle.

Site name	Elevation (m)	TROPOMI SIF			FLUXCOM GPP			CLM5.0-BGC GPP			CLM5.0-SP GPP		
		$t_{\text{EC,peak}} - t_{\text{SIF,peak}}$ (months)	$t_{\text{EC,cycle}} - t_{\text{SIF,cycle}}$ (months)	Lag R^2	$t_{\text{EC,peak}} - t_{\text{GPP,peak}}$ (months)	$t_{\text{EC,cycle}} - t_{\text{GPP,cycle}}$ (months)	Lag R^2	$t_{\text{EC,peak}} - t_{\text{GPP,peak}}$ (months)	$t_{\text{EC,cycle}} - t_{\text{GPP,cycle}}$ (months)	Lag R^2	$t_{\text{EC,peak}} - t_{\text{GPP,peak}}$ (months)	$t_{\text{EC,cycle}} - t_{\text{GPP,cycle}}$ (months)	Lag R^2
US-CZ4	2700	0	1	0.45	0	1	0.89	1	2	0.75	0	1	0.83
TEAK	2147	-1	0	0.56	-1	0	0.91	0	1	0.84	-1	0	0.94
US-CZ3	2015	-1	-1	0.76	-2	-1	0.77	0	0	0.84	0	0	0.88
US-CZ2	1160	0	0	0.81	0	-1	0.84	2	2	0.77	1	1	0.74

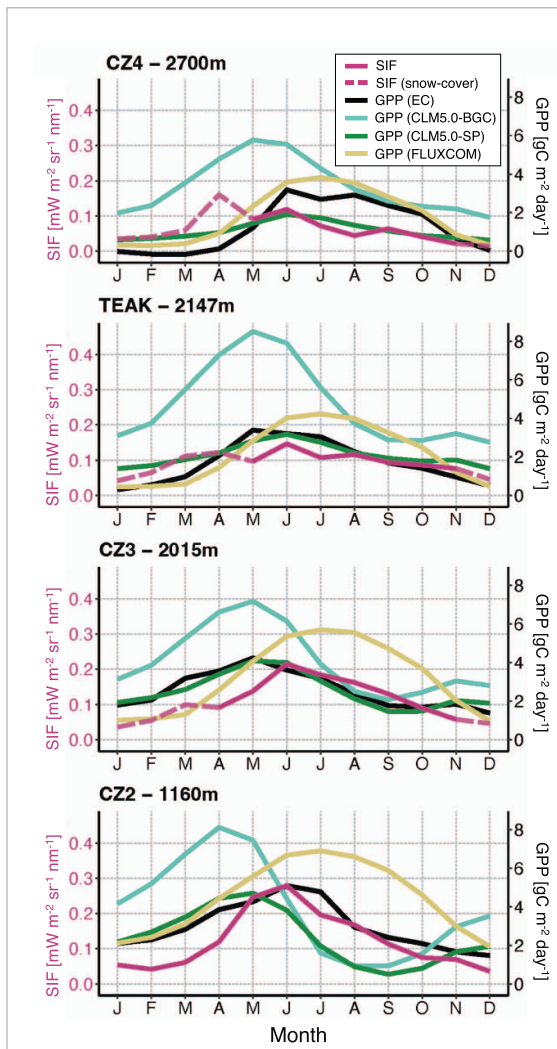


Figure 5. Comparison of mean seasonal cycles: TROPOMI SIF (red), EC GPP (black), modeled GPP from CLM5.0-BGC (light green), CLM5.0-SP (dark green) and FLUXCOM GPP (yellow). Comparisons are shown at each of the four flux tower sites along the Sierra Nevada elevational transect. SIF is shown in dashed lines, where the mean MODIS snow cover fraction was over 50%, to denote periods where SIF was omitted from the analysis due to noise from high reflected radiance. All seasonal cycles represent the multi-year average across their respective available time ranges listed in table 1.

FLUXCOM GPP timing was close to that of EC GPP at high elevation sites but was up to 2 months delayed from EC GPP at lower elevations. CLM5.0-BGC was the least synchronous with EC GPP timing, often 2 months offset from ground-based estimates.

4. Discussion

4.1. Patterns of GPP and SIF compared to expected limitations

The elevational and seasonal trends of TROPOMI SIF, FLUXCOM GPP and CLM5.0-SP (figures 3(a-c)) largely align with the ecological expectations for environmental limitations on GPP described in figure 1 and in the climate and land cover datasets used here.

4.1.1. Temperature limitation

The daily mean winter temperature threshold for strong cold limitation along the Sierra Nevada flux tower transect is likely somewhere between 2.5 °C (winter-dormant 2700 m site) and 6.3 °C (winter-active 2015 m site) (Goulden *et al* 2012). This occurs between 1500 and 2000 m elevation in December–January according to the GRIDMET modeled temperature across the Sierra Nevada study region (figure 3(e)). Both CLM5.0-SP and FLUXCOM GPP suggest a significant transition between 1500 and 2000 m in winter, with negligible GPP above 2000 m from December to March (figure 3(b)), following Goulden *et al* (2012). In contrast, the modeled GPP from CLM5.0-BGC showed virtually no winter dormancy, except above 3000 m. Although winter-time SIF could not be effectively analyzed due to snow contamination, these results demonstrate consistency between gridded GPP and the existing literature for winter patterns in the Sierra Nevada.

During summer, the 90th percentile of gridded SIF corresponds to the GRIDMET mean air temperature (18 °C–19 °C) near or within the optimal temperature range reported in global synthesis studies (~15 °C–20 °C per Duffy *et al* (2021), 18 °C–20 °C for ENF per Chen *et al* (2023), and ~13 °C–17 °C for ENF per Huang *et al* (2019)). The 90th percentile of FLUXCOM GPP corresponds to a much higher temperature range (17 °C–24 °C) than in these studies, suggesting that the peak growing season in FLUXCOM is biased late into the hot summer. Conversely, the peak modeled GPP from CLM5.0 occurs at cooler elevations and months (7 °C–14 °C for SP and 4 °C–12 °C for BGC), which we attribute to a slight early-season bias in CLM5.0-SP and an early-season high-elevation bias for CLM5.0-BGC linked to patterns in simulated LAI.

4.1.2. Moisture limitation

TerraClimate-modeled CWD is strongly seasonal and greatest in late summer (figure 3(f)); however, patterns in CWD are not necessarily consistent with observations, given that numerous studies (Goulden *et al* 2012, Kelly and Goulden 2016, O'Geen *et al* 2018, Rungee *et al* 2019) have observed the capacity of the mid-elevation Sierra Nevada forests to maintain GPP and ET throughout the summer. This is because roots can reach at least 5 m deep (Kelly and Goulden 2016), allowing consistent access to subsurface water storage.

Our findings suggest that moisture limitation may still have an impact on seasonal GPP in the Sierra Nevada, depending on the elevation. A distinct late-season bias in FLUXCOM is apparent compared to flux tower GPP at low to mid-elevations (figure 5, table 2) and compared to SIF and modeled GPP (figure 4(b)), which we suspect is caused by the underestimation of water stress effects in FLUXCOM. Conversely, CLM5.0-SP generally matches EC GPP

timing (figure 5) and is well constrained by moisture limitation, particularly between 1000 and 2000 m (appendix C). The lowest site (1160 m) is an exception, with higher seasonal EC GPP compared to CLM5.0-SP, suggesting a balance between seasonal drought and deep subsurface water access. Although CLM5.0 represents both rooting depth and subsurface hydrology, it does not represent deep roots (>1 m) that have access to water. SIF, on the other hand, most closely matches EC GPP timing at 1160 m, indicating that SIF may indeed capture seasonal moisture limitation.

4.1.3. Vegetation density limitation

Above the mid-elevation range (~ 1500 m), we expect vegetation density to be a major limitation to GPP during peak growing season, noting a relatively consistent LAI gradient of -1.1 (-38%) per kilometer in elevation. The elevational gradients of TROPOMI SIF, FLUXCOM GPP and CLM5.0-SP scale proportionally to LAI in July at -40% , -33% and -43% per kilometer, respectively. The model-simulated LAI in CLM5.0-BGC caused unrealistically high GPP at high elevations, diverging substantially from the expected vegetation density-driven elevational patterns. Unlike the other models, CLM5.0-BGC was not calibrated with LAI observations for the Sierra Nevada mountain range. Thus, we did not expect CLM-BGC to perform as well. Flux tower GPP has a slightly milder elevational gradient in July (-28% per kilometer elevation from 1160 to 2700 m sites), although we speculate that the 2700 m EC site likely exhibits higher LAI than average for that elevation due to its selection as a forest EC site. Overall, there is a strong similarity between the elevational gradients of LAI, SIF and GPP during the peak growing season, aligning with expectations (figure 1).

4.2. Comparison of mean seasonal cycles

The timing of the spring onset and June–July peak of TROPOMI SIF and FLUXCOM GPP (figure 4(b)) agree with previous studies of ENF GPP in the Sierra Nevada (Goldstein *et al* 2000, Misson *et al* 2006, Goulden *et al* 2012). Our findings of TROPOMI SIF seasonality are similar to the results of Turner *et al* (2020) across California, which showed peak TROPOMI SIF from ENF between June and July. FLUXCOM GPP seasonality generally matched other FLUXCOM studies (Byrne *et al* 2018 (ENF); Sun *et al* 2018), although the FLUXCOM GPP shown here is comparatively high in fall. The most significant deviation between TROPOMI SIF and FLUXCOM occurred after the initial peak in June (figure 4(b)), when SIF declined sharply and FLUXCOM GPP remained high throughout the summer and into the fall, during which we would expect water stress to limit GPP to some extent (section 4.1). Similar seasonal deviations between TROPOMI SIF and FLUXCOM GPP have been documented (e.g. Chen

et al 2021b). We suspect that these deviations reflect the strong coupling of FLUXCOM GPP to MODIS vegetation indices (NDVI, EVI, NIR_v, etc) during summer and early fall (figure A2). However, TROPOMI SIF captured the expected seasonal down-regulation of photosynthesis much more effectively than the other satellite-based vegetation indices. As a result, the seasonal and elevational patterns of TROPOMI SIF and FLUXCOM GPP were more highly correlated than any other gridded GPP comparison, including comparisons with NIR_v, EVI, NDVI, etc (see appendix A).

In theory, flux tower observations should serve to further connect these global gridded datasets to local patterns of GPP. The mean seasonalities of TROPOMI SIF and CLM5.0-SP were both consistently within 1 month of the mean EC GPP seasonality, whereas the mean seasonality of FLUXCOM GPP was consistently delayed from EC GPP. This helps explain the significant summer–fall deviations between the TROPOMI and FLUXCOM signals, providing more confidence that TROPOMI SIF appropriately tracks the timing of GPP across the Sierra Nevada elevational gradient.

4.3. Limitations and applications to carbon monitoring systems

Functional carbon monitoring systems across the western US will need to rely on robust connections between ground- and satellite-based data over complex terrain. In addition to SIF, other remote-sensing and ground-based data streams will help further elucidate biophysical (e.g. NDVI and NIR_v), biochemical (e.g. photochemical reflectance index (Gamon *et al* 1997) and chlorophyll/carotenoid index (Gamon *et al* 2016)) and hydrologic (e.g. soil moisture and snow cover) processes. Nonetheless, there is burgeoning scientific interest in satellite-based SIF for carbon monitoring and early stress detection, so far mostly in agricultural systems (Zhang *et al* 2019, 2023, Peng *et al* 2020, Sloat *et al* 2021, Mohammadi *et al* 2022). A growing body of evidence points toward the linearity of the SIF–GPP relationship at seasonal canopy scales (Frankenberg *et al* 2011, Yang *et al* 2015, Li and Xiao 2019, Magney *et al* 2020). Future research is needed to determine how the time series of SIF over ENF biomes correlate with carbon fluxes over ecologically meaningful timescales (years to decades). To this end, several limitations are important to consider.

4.3.1. SIF and land cover

The relatively low signal-to-noise ratio of satellite-based SIF will remain a limitation, requiring averaging in space and/or time to increase precision. We found that snow cover was a large source of noise in the satellite SIF, introducing a large positive bias into the SIF signal. Highly reflective and heterogeneous land cover also has strong effects on signal-to-noise SIF ratios (Köhler *et al* 2018, Cheng *et al* 2022b).

High-resolution land cover and disturbance datasets will be useful to help identify and separate these influences from overall biome trends, but users must be aware of the sub-grid scale heterogeneity and classification uncertainty. One must also consider the changing seasonal role of environmental drivers (snow, soil moisture, heat and APAR), which have been shown to have asymmetric impacts on the SIF–GPP relationship even at the satellite scale (Chen *et al* 2021a).

4.3.2. GPP

Model-data estimates of GPP (e.g. FLUXCOM) are useful for areas without significant EC data coverage. However, one must consider the impact of extrapolation of these estimates to under-sampled heterogeneous terrain. It is also important to consider that analyses of EC GPP in heterogeneous terrain are ultimately influenced by site selection, as well as the averaging period and grid resolution of the comparison datasets. For example, the EC data at the 1160 m site were significantly impacted by drought-induced disturbance from 2013 to the present (Goulden and Bales 2019, appendix B). However, typical EC footprints are small relative to many satellite data scales (e.g. <5% of the original TROPOMI sampling area). Thus, disturbances may be impactful at the EC scale but negligible at the satellite scale, or vice versa. This exemplifies the challenges in tower-satellite representation, which are well described in other vegetation remote-sensing studies (e.g. Yu and Ma 2015, Lu *et al* 2018, Schimel and Schneider 2019, Du *et al* 2023), particularly those within complex terrain (Desai *et al* 2011).

4.3.3. Terrestrial biosphere models

Fully prognostic land surface models, such as CLM-BGC, have well-documented shortcomings in capturing vegetation phenology (e.g. mischaracterized rooting depth and uncaptured winter dormancy; Richardson *et al* 2012, Raczka *et al* 2016, 2019), which, to some extent, we have addressed here through the prescription of LAI observations into CLM5-SP. In general, systematic biases in land surface models due to deficiencies in process representation cannot be fully addressed through the implementation of fine-scale land surface and atmospheric forcing data alone (Duarte *et al* 2022). Future work intends to utilize model-data fusion techniques, such as ensemble data assimilation (Raczka *et al* 2021), to leverage satellite observations (SIF, leaf area and snow cover) and recent canopy-level SIF representation in CLM (Li *et al* 2022).

5. Conclusion

Satellite remote sensing of vegetation will be integral to the development of carbon flux monitoring systems, both globally and regionally, with montane

evergreen conifer forests in the western US presenting unique challenges to monitoring goals at these scales. Here, we assessed the ability of high-resolution satellite SIF to track the average trends of photosynthesis across seasons and elevations in one of the largest and most dynamic mountain ranges in the western US. After filtering for snow-covered surfaces, TROPOMI SIF showed strong agreement in elevational patterns with a robust model-data GPP product (FLUXCOM) and a data-constrained land surface model (CLM5.0-SP) while closely matching the mean seasonal timing of EC tower GPP across four flux monitoring sites in the Sierra Nevada. We also found that, compared to active biogeochemistry (CLM5.0-BGC) simulations, modeled GPP constrained by satellite phenology (CLM5.0-SP) showed substantially better agreement with EC GPP. The spatial mismatch between EC and gridded satellite data, combined with localized disturbance events, presents challenges for tower-to-satellite-scale comparisons. Nonetheless, SIF and FLUXCOM GPP were more highly correlated across elevations and seasons than any other combination of gridded GPP and satellite vegetation indices. These findings provide strong evidence that satellite-based SIF can provide unique and valuable information to carbon monitoring systems over mountainous ENF regions, such as the western US, particularly when integrated with data assimilation techniques.

Data availability statements

The eddy covariance data were provided by the AmeriFlux Network and the National Ecological Observatory Network (NEON). NEON is a program sponsored by the National Science Foundation and operated under the cooperative agreement of Battelle. This material is based in part on work supported by the National Science Foundation through the NEON program.

The data that support the findings of this study are openly available at the following URL/DOI: <https://doi.org/10.5281/zenodo.8239702>.

Acknowledgments

This research was funded by the NASA Carbon Monitoring Systems program Award 80NSSC20K0010 and the National Science Foundation Graduate Research Fellowship Program Award #2139322. Additional funding was provided by the US National Science Foundation Macrosystems Biology and NEON-Enabled Science (Award 1926090) and Division of Environmental Biology (Award 1929709) programs.

Conflict of interest

The authors have no competing interests to declare.

ORCID iDs

Lewis Kunik  <https://orcid.org/0000-0001-9638-0543>

David R Bowling  <https://orcid.org/0000-0002-3864-4042>

Brett Raczka  <https://orcid.org/0000-0003-0582-1118>

Christian Frankenberg  <https://orcid.org/0000-0002-0546-5857>

Philipp Köhler  <https://orcid.org/0000-0002-7820-1318>

Rui Cheng  <https://orcid.org/0000-0002-3003-8339>

Kenneth R Smith  <https://orcid.org/0000-0003-1966-3042>

Michael Goulden  <https://orcid.org/0000-0002-9379-3948>

John C Lin  <https://orcid.org/0000-0003-2794-184X>

References

Abatzoglou J T 2013 Development of gridded surface meteorological data for ecological applications and modelling *Int. J. Climatol.* **33** 121–31

Abatzoglou J T, Dobrowski S Z, Parks S A and Hegewisch K C 2018 TerraClimate, a high-resolution global dataset of monthly climate and climatic water balance from 1958–2015 *Sci. Data* **5** 170191

Adams M B, Kelly C, Kabrick J and Schuler J 2019 Temperate forests and soils *Developments in Soil Science* vol 36 ed M Busse, C P Giardina, D M Morris and D S Page-Dumroese (Elsevier) ch 6, pp 83–108

Amante C and Eakins B 2009 ETOPO1 1 arc-minute global relief model: procedures, data sources and analysis (<https://doi.org/10.7289/V5C8276M>)

Angert A, Biraud S, Bonfils C, Henning C C, Buermann W, Pinzon J, Tucker C J and Fung I 2005 Drier summers cancel out the CO₂ uptake enhancement induced by warmer springs *Proc. Natl Acad. Sci.* **102** 10823–7

Baldocchi D 2008 Breathing of the terrestrial biosphere: lessons learned from a global network of carbon dioxide flux measurement systems *Aust. J. Bot.* **56** 1–26

Buotte P C, Lewis S, Law B E, Hudiburg T W, Rupp D E and Kent J J 2019 Near-future forest vulnerability to drought and fire varies across the western United States *Glob. Change Biol.* **25** 290–303

Butterfield Z, Magney T, Grossmann K, Bohrer G, Vogel C, Barr S and Keppel-Aleks G 2023 Accounting for changes in radiation improves the ability of SIF to track water stress-induced losses in summer GPP in a temperate deciduous forest *J. Geophys. Res.* **128** e2022JG007352

Byrne B *et al* 2018 Evaluating GPP and respiration estimates over northern midlatitude ecosystems using solar-induced fluorescence and atmospheric CO₂ measurements *J. Geophys. Res.* **123** 2976–97

Chen A, Mao J, Ricciuto D, Lu D, Xiao J, Li X, Thornton P E and Knapp A K 2021a Seasonal changes in GPP/SIF ratios and their climatic determinants across the Northern Hemisphere *Glob. Change Biol.* **27** 5186–97

Chen A, Mao J, Ricciuto D, Xiao J, Frankenberg C, Li X, Thornton P E, Gu L and Knapp A K 2021b Moisture availability mediates the relationship between terrestrial gross primary production and solar-induced chlorophyll fluorescence: insights from global-scale variations *Glob. Change Biol.* **27** 1144–56

Chen W, Wang S, Wang J, Xia J, Luo Y, Yu G and Niu S 2023 Evidence for widespread thermal optimality of ecosystem respiration *Nat. Ecol. Evol.* **7** 1379–87

Cheng R, Köhler P and Frankenberg C 2022a Impact of radiation variations on temporal upscaling of instantaneous solar-induced chlorophyll fluorescence *Agric. For. Meteorol.* **327** 109197

Cheng R *et al* 2022b Evaluating photosynthetic activity across Arctic-Boreal land cover types using solar-induced fluorescence *Environ. Res. Lett.* **17** 115009

Chu H *et al* 2021 Representativeness of eddy-covariance flux footprints for areas surrounding AmeriFlux sites *Agric. For. Meteorol.* **301–2** 108350

Clark J S *et al* 2016 The impacts of increasing drought on forest dynamics, structure, and biodiversity in the United States *Glob. Change Biol.* **22** 2329–52

Daly C, Halbleib M, Smith J I, Gibson W P, Doggett M K, Taylor G H, Curtis J and Pasteris P P 2008 Physiographically sensitive mapping of climatological temperature and precipitation across the conterminous United States *Int. J. Climatol.* **28** 2031–64

Danabasoglu G *et al* 2020 The community earth system model version 2 (CESM2) *J. Adv. Model. Earth Syst.* **12** e2019MS001916

Desai A R *et al* 2011 Seasonal pattern of regional carbon balance in the central Rocky Mountains from surface and airborne measurements *J. Geophys. Res.* **116** G04009

Du S, Liu X, Chen J, Duan W and Liu L 2023 Addressing validation challenges for TROPOMI solar-induced chlorophyll fluorescence products using tower-based measurements and an NIRv-scaled approach *Remote Sens. Environ.* **290** 113547

Duarte H F, Raczka B M, Bowling D R, Wang A, Buotte P C and Lin J C 2022 How can biosphere models simulate enough vegetation biomass in the mountains of the western United States? Implications of meteorological forcing *Environ. Model. Softw.* **148** 105288

Duffy K A, Schwalm C R, Arcus V L, Koch G W, Liang L L and Schipper L A 2021 How close are we to the temperature tipping point of the terrestrial biosphere? *Sci. Adv.* **7** eaay1052

Fettig C J, Hood S M, Runyon J B and Stalling C M 2021 Bark beetle and fire interactions in western coniferous forests: research findings *Fire Manage. Today* **79** 10

Frankenberg C *et al* 2011 New global observations of the terrestrial carbon cycle from GOSAT: patterns of plant fluorescence with gross primary productivity *Geophys. Res. Lett.* **38** L17706

Gamon J A, Huemmrich K F, Wong C Y S, Ensminger I, Garrity S, Hollinger D Y, Noormets A and Peñuelas J 2016 A remotely sensed pigment index reveals photosynthetic phenology in evergreen conifers *Proc. Natl Acad. Sci.* **113** 13087–92

Gamon J A, Serrano L and Surfus J S 1997 The photochemical reflectance index: an optical indicator of photosynthetic radiation use efficiency across species, functional types, and nutrient levels *Oecologia* **112** 492–501

Goldstein A H, Hultman N E, Fracheboud J M, Bauer M R, Panek J A, Xu M, Qi Y, Guenther A B and Baugh W 2000 Effects of climate variability on the carbon dioxide, water, and sensible heat fluxes above a ponderosa pine plantation in the Sierra Nevada (CA) *Agric. For. Meteorol.* **101** 113–29

Goulden M L, Anderson R G, Bales R C, Kelly A E, Meadows M and Winston G C 2012 Evapotranspiration along an elevation gradient in California's Sierra Nevada *J. Geophys. Res.* **117** G03028

Goulden M L and Bales R C 2019 California forest die-off linked to multi-year deep soil drying in 2012–2015 drought *Nat. Geosci.* **12** 632–7

Goulden M 2018a AmeriFlux BASE US-CZ2 sierra critical zone, sierra transect, ponderosa pine forest, soaproot saddle, ver. 1–5 AmeriFlux AMP (<https://doi.org/10.17190/AMF/1419510>)

Goulden M 2018b AmeriFlux BASE US-CZ3 sierra critical zone, sierra transect, sierran mixed conifer, P301, ver. 1–5 *AmeriFlux AMP* (<https://doi.org/10.17190/AMF/1419512>)

Goulden M 2018c AmeriFlux BASE US-CZ4 sierra critical zone, sierra transect, subalpine forest, shorthair, ver. 1–5 *AmeriFlux AMP* (<https://doi.org/10.17190/AMF/1419511>)

Guanter L *et al* 2014 Global and time-resolved monitoring of crop photosynthesis with chlorophyll fluorescence *Proc. Natl Acad. Sci.* **111** E1327–33

Hall D K and Riggs G A 2021 MODIS/terra snow cover monthly L3 global 0.05Deg CMG, version 61 (Distributed by NASA National Snow and Ice Data Center Distributed Active Archive Center) (<https://doi.org/10.5067/MODIS/MOD10CM.061>) (Accessed 16 July 2023)

Helm L T, Shi H, Lerdau M T and Yang X 2020 Solar-induced chlorophyll fluorescence and short-term photosynthetic response to drought *Ecol. Appl.* **30** e02101

Hollman R *et al* 2013 The ESA climate change initiative: satellite data records for essential climate variables *Bull. Am. Meteorol. Soc.* **94** 1541–52

Huang M *et al* 2019 Air temperature optima of vegetation productivity across global biomes *Nat. Ecol. Evol.* **3** 372–9

Intergovernmental Panel on Climate Change (IPCC) 2023 *Climate Change 2021 – The Physical Science Basis: Working Group I Contribution to the Sixth Assessment Report of the Intergovernmental Panel on Climate Change* (Cambridge University Press) (<https://doi.org/10.1017/9781009157896>)

Jung M *et al* 2020 Scaling carbon fluxes from eddy covariance sites to globe: synthesis and evaluation of the FLUXCOM approach *Biogeosciences* **17** 1343–65

Kelly A E and Goulden M L 2016 A montane Mediterranean climate supports year-round photosynthesis and high forest biomass *Tree Physiol.* **36** tpv131

Köhler P, Frankenberg C, Magney T S, Guanter L, Joiner J and Landgraf J 2018 Global retrievals of solar-induced chlorophyll fluorescence with TROPOMI: first results and intersensor comparison to OCO-2 *Geophys. Res. Lett.* **45** 10,456–63

Lawrence D M *et al* 2019 The community land model version 5: description of new features, benchmarking, and impact of forcing uncertainty *J. Adv. Model. Earth Syst.* **11** 4245–87

Li R, Lombardozzi D, Shi M, Frankenberg C, Parazoo N C, Köhler P, Yi K, Guan K and Yang X 2022 Representation of leaf-to-canopy radiative transfer processes improves simulation of far-red solar-induced chlorophyll fluorescence in the community land model version 5 *J. Adv. Model. Earth Syst.* **14** e2021MS002747

Li X and Xiao J 2019 Mapping photosynthesis solely from solar-induced chlorophyll fluorescence: a global, fine-resolution dataset of gross primary production derived from OCO-2 *Remote Sens.* **11** 2563

Lu X, Cheng X, Li X and Tang J 2018 Opportunities and challenges of applications of satellite-derived sun-induced fluorescence at relatively high spatial resolution *Sci. Total Environ.* **619–20** 649–53

Magney T S *et al* 2019 Mechanistic evidence for tracking the seasonality of photosynthesis with solar-induced fluorescence *Proc. Natl Acad. Sci.* **116** 11640–5

Magney T S, Barnes M L and Yang X 2020 On the covariation of chlorophyll fluorescence and photosynthesis across scales *Geophys. Res. Lett.* **47** e2020GL091098

Marrs J K, Reblin J S, Logan B A, Allen D W, Reinmann A B, Bombard D M, Tabachnik D and Hutyra L R 2020 Solar-induced fluorescence does not track photosynthetic carbon assimilation following induced stomatal closure *Geophys. Res. Lett.* **47** e2020GL087956

Metzger S *et al* 2019 From NEON field sites to data portal: a community resource for surface–atmosphere research comes online *Bull. Am. Meteorol. Soc.* **100** 2305–25

Misson L, Tu K, Boniello R A and Goldstein A H 2006 Seasonally of photosynthetic parameters in a multi-specific and vertically complex forest ecosystem in the Sierra Nevada of California *Tree Physiol.* **26** 729–41

Mitchell K E *et al* 2004 The multi-institution North American Land Data Assimilation System (NLDAS): utilizing multiple GCIP products and partners in a continental distributed hydrological modeling system *J. Geophys. Res.* **109** D07S90

Mohammadi K, Jiang Y and Wang G 2022 Flash drought early warning based on the trajectory of solar-induced chlorophyll fluorescence *Proc. Natl Acad. Sci.* **119** e2202767119

Monteith J L 1972 Solar radiation and productivity in tropical ecosystems *J. Appl. Ecol.* **9** 747–66

Myneni R, Knyazikhin Y and Park T 2021 MODIS/terra+aqua leaf area index/FPAR 8-day L4 global 500 m SIN grid V061 (NASA EOSDIS Land Processes DAAC) (<https://doi.org/10.5067/MODIS/MCD15A2H.061>) (Accessed 15 July 2023)

NEON (National Ecological Observatory Network) 2022 Bundled data products—eddy covariance (DP4.00200.001) (<https://doi.org/10.48443/7cqp-3j73>)

O'Geen A T *et al* 2018 Southern sierra critical zone observatory and kings river experimental watersheds: a synthesis of measurements, new insights, and future directions *Zone J.* **17** 180081

Oswalt S N, Smith W B, Miles P D and Pugh S A 2019 Forest resources of the United States, 2017: a technical document supporting the forest service 2020 RPA assessment *Gen. Tech. Rep. WO-97* (U.S. Department of Agriculture, Forest Service, Washington Office) (<https://doi.org/10.2737/WO-GTR-97>)

Pastorello G *et al* 2020 The FLUXNET2015 dataset and the ONEFlux processing pipeline for eddy covariance data *Sci. Data* **7** 225

Peng B, Guan K, Zhou W, Jiang C, Frankenberg C, Sun Y, He L and Köhler P 2020 Assessing the benefit of satellite-based solar-induced chlorophyll fluorescence in crop yield prediction *Int. J. Appl. Earth Obs. Geoinf.* **90** 102126

Pierrat Z A *et al* The biological basis for using optical signals to track evergreen needleleaf photosynthesis *BioScience* in review

Pierrat Z *et al* 2022 Diurnal and seasonal dynamics of solar-induced chlorophyll fluorescence, vegetation indices, and gross primary productivity in the boreal forest *J. Geophys. Res.* **127** e2021JG006588

Potter D 1998 Forested communities of the upper montane in the central and Southern Sierra Nevada (Retrieved 8 May 2023) (available at: www.fs.usda.gov/psw/publications/documents/psw_gtr169/)

Raczka B *et al* 2019 Sustained nonphotochemical quenching shapes the seasonal pattern of solar-induced fluorescence at a high-elevation evergreen forest *J. Geophys. Res.* **124** 2005–20

Raczka B, Duarte H F, Koven C D, Ricciuto D, Thornton P E, Lin J C and Bowling D R 2016 An observational constraint on stomatal function in forests: evaluating coupled carbon and water vapor exchange with carbon isotopes in the community land model (CLM4.5) *Biogeosciences* **13** 5183–204

Raczka B, Hoar T J, Duarte H F, Fox A M, Anderson J L, Bowling D R and Lin J C 2021 Improving CLM5.0 biomass and carbon exchange across the western United States using a data assimilation system *J. Adv. Model. Earth Syst.* **13** e2020MS002421

Reichstein M *et al* 2005 On the separation of net ecosystem exchange into assimilation and ecosystem respiration: review and improved algorithm *Glob. Change Biol.* **11** 1424–39

Richardson A D *et al* 2012 Terrestrial biosphere models need better representation of vegetation phenology: results from the North American carbon program site synthesis *Glob. Change Biol.* **18** 566–84

Rotach M W, Wohlfahrt G, Hansel A, Reif M, Wagner J and Gohm A 2014 The world is not flat: implications for the global carbon balance *Bull. Am. Meteorol. Soc.* **95** 1021–8

Rungee J, Bales R and Goulden M 2019 Evapotranspiration response to multiyear dry periods in the semiarid western United States *Hydrol. Process.* **33** 182–94

Schimel D T, Kittel G F, Running S, Monson R, Turnipseed A and Anderson D 2002 Carbon sequestration studied in western U.S. mountains *EOS Trans.* **83** 445, 449

Schimel D and Braswell B H 2005 The role of mid-latitude mountains in the carbon cycle: global perspective and a western US case study *Global Change and Mountain Regions: An Overview of Current Knowledge* ed U M Huber, H K M Bugmann and M A Reasoner pp 449–56

Schimel D and Schneider F D 2019 Flux towers in the sky: global ecology from space *New Phytol. JPL Carbon and Ecosystem Participants* **224** 570–84

Shulgina T *et al* 2023 Observed and projected changes in snow accumulation and snowline in California's snowy mountains *Clim. Dyn.* **61** 4809–24

Sirila-Woodburn E R *et al* 2021 A low-to-no snow future and its impacts on water resources in the western United States *Nat. Rev. Earth Environ.* **2** 800–19

Sloat L L, Lin M, Butler E E, Johnson D, Holbrook N M, Huybers P J, Lee J-E and Mueller N D 2021 Evaluating the benefits of chlorophyll fluorescence for in-season crop productivity forecasting *Remote Sens. Environ.* **260** 112478

Sun Y *et al* 2017 OCO-2 advances photosynthesis observation from space via solar-induced chlorophyll fluorescence *Science* **358** eaam5747

Sun Y, Frankenberg C, Jung M, Joiner J, Guanter L, Köhler P and Magney T 2018 Overview of solar-induced chlorophyll fluorescence (SIF) from the orbiting carbon observatory-2: retrieval, cross-mission comparison, and global monitoring for GPP *Remote Sens. Environ.* **209** 808–23

Sun Y, Fu R, Dickinson R, Joiner J, Frankenberg C, Gu L, Xia Y and Fernando N 2015 Drought onset mechanisms revealed by satellite solar-induced chlorophyll fluorescence: insights from two contrasting extreme events *J. Geophys. Res.* **120** 2015JG003150

Tramontana G *et al* 2016 Predicting carbon dioxide and energy fluxes across global FLUXNET sites with regression algorithms *Biogeosciences* **13** 4291–313

Trujillo E, Molotch N P, Goulden M L, Kelly A E and Bales R C 2012 Elevation-dependent influence of snow accumulation on forest greening *Nat. Geosci.* **5** 705–9

Turner A J, Köhler P, Magney T S, Frankenberg C, Fung I and Cohen R C 2020 A double peak in the seasonality of California's photosynthesis as observed from space *Biogeosciences* **17** 405–22

Walther S, Voigt M, Thum T, Gonsamo A, Zhang Y, Köhler P, Jung M, Varlagin A and Guanter L 2016 Satellite chlorophyll fluorescence measurements reveal large-scale decoupling of photosynthesis and greenness dynamics in boreal evergreen forests *Glob. Change Biol.* **22** 2979–96

Wutzler T, Lucas-Moffat A, Migliavacca M, Knauer J, Sickel K, Šigut L, Menzer O and Reichstein M 2018 Basic and extensible post-processing of eddy covariance flux data with REddyProc *Biogeosciences* **15** 5015–30

Yang J C *et al* 2022 Gross primary production (GPP) and red solar induced fluorescence (SIF) respond differently to light and seasonal environmental conditions in a subalpine conifer forest *Agric. For. Meteorol.* **317** 108904

Yang X, Tang J W, Mustard J F, Lee J E, Rossini M, Joiner J, Munger J W, Kornfeld A and Richardson A D 2015 Solar-induced chlorophyll fluorescence that correlates with canopy photosynthesis on diurnal and seasonal scales in a temperate deciduous forest *Geophys. Res. Lett.* **42** 2977–87

Yu W and Ma M 2015 Scale mismatch between *in situ* and remote sensing observations of land surface temperature: implications for the validation of remote sensing LST products *IEEE Geosci. Remote. Sens.* **12** 497–501

Zeng Y, Badgley G, Dechant B, Ryu Y, Chen M and Berry J A 2019 A practical approach for estimating the escape ratio of near-infrared solar-induced chlorophyll fluorescence *Remote Sens. Environ.* **232** 111209

Zhang L, Qiao N, Huang C and Wang S 2019 Monitoring drought effects on vegetation productivity using satellite solar-induced chlorophyll fluorescence *Remote Sens.* **11** 378

Zhang Y, Fang J, Smith W K, Wang X, Gentine P, Scott R L, Migliavacca M, Jeong S, Litvak M and Zhou S 2023 Satellite solar-induced chlorophyll fluorescence tracks physiological drought stress development during 2020 southwest US drought *Glob. Change Biol.* **29** 3395–408

Zuromski L M, Bowling D R, Köhler P, Frankenberg C, Goulden M L, Blanken P D and Lin J C 2018 Solar-induced fluorescence detects interannual variation in gross primary production of coniferous forests in the western United States *Geophys. Res. Lett.* **45** 7184–93